

An adaptive stabilized trace finite element method for surface PDEs

Timo Heister*

Maxim A. Olshanskii[†]

Vladimir Yushutin*

August 21, 2024

Abstract

The paper introduces an adaptive version of the stabilized Trace Finite Element Method (TraceFEM) designed to solve low-regularity elliptic problems on level-set surfaces using a shape-regular bulk mesh in the embedding space. Two stabilization variants, gradient-jump face and normal-gradient volume, are considered for continuous trace spaces of the first and second degrees, based on the polynomial families Q_1 and Q_2 . We propose a practical error indicator that estimates the ‘jumps’ of finite element solution derivatives across background mesh faces and it avoids integration of any quantities along implicitly defined curvilinear edges of the discrete surface elements. For the Q_1 family of piecewise trilinear polynomials on bulk cells, the solve-estimate-mark-refine strategy, combined with the suggested error indicator, achieves optimal convergence rates typical of two-dimensional problems. We also provide a posteriori error estimates, establishing the reliability of the error indicator for the Q_1 and Q_2 elements and for two types of stabilization. In numerical experiments, we assess the reliability and efficiency of the error indicator. While both stabilizations are found to deliver comparable performance, the lowest degree finite element space appears to be the more robust choice for the adaptive TraceFEM framework.

Keywords: Surface, PDE, finite elements, traces, unfitted grid, adaptivity, level set, stabilization

1 Introduction

The Trace or Cut Finite Element Method is one of the approaches used to approximate surface Partial Differential Equations (PDEs) [1, 2]. It falls into the category of geometrically unfitted methods because the domain of a variational problem, a two-dimensional surface denoted as Γ , is embedded within a three-dimensional triangulated domain Ω that is a subset of \mathbb{R}^3 , such as a sufficiently large cube. Identifying the active mesh, denoted as $\Omega_h \subset \Omega$, and performing local refinement or any other mesh cell updating procedure is straightforward due to the geometrical simplicity. We refer to Figure 1 for a visual representation. Furthermore, handling data structures on the octree mesh Ω_h can be implemented efficiently and is available in many finite element libraries. This flexibility is one of the advantages of the Trace Finite Element Method (TraceFEM). However, it comes with the cost of constructing quadratures on the intersections of Γ with cells from Ω_h . The size and shape of these intersections vary uncontrollably between cells, leading to the necessity for a stabilization term, similar to s_h in equation (1), in any TraceFEM discretization of surface problems. Several variants of such terms are available in the literature [1, 3], but in this context, we will only consider the ‘gradient-jump’ face stabilization and the ‘normal-gradient’ volume stabilization. These methods have been successfully used and proven to be practical and robust.

Adaptive strategies within the context of stabilized TraceFEM are not yet well-understood. Previous discussions on adaptivity in the TraceFEM setting can be found in the literature [4, 5]. In [4], there is no stabilization, and an inferior (as seen in the comparison in [1]) ‘full-gradient’ stabilization is considered in [5]. Additionally, both papers only considered piece-wise linear finite element spaces, with [4] assuming tetrahedral meshes and [5] using octree meshes. We extend the adaptive methodology introduced in [4] by

*School of Mathematical and Statistical Sciences, Clemson University, Clemson, SC 29634-0975, USA, heister@clemson.edu, vyushut@clemson.edu.

[†]Department of Mathematics, University of Houston, Houston, Texas 77204-3008, USA maolshanskiy@uh.edu, www.math.uh.edu/~molshan

studying the first and second-order stabilized TraceFEM on octree meshes. Another novel aspect is the consideration of two stabilizations, namely s_h^{JF} (as defined in (11)) and s_h^{NV} (as defined in (13)), in the context of adaptive TraceFEM.

Many mathematical models involving surface PDEs necessitate the use of adaptive numerical methods. For instance, the dynamics of liquid crystal films can give rise to the formation of defects [6, 7, 8, 9]. Mathematically, a defect in a liquid crystal film corresponds to low regularity solutions of the governing PDEs on surfaces. From a numerical modeling perspective, this entails the need for adaptive refinement and coarsening as the defect forms and evolves along the film. The evolution of defects is driven by variations in the energy of the liquid crystal and the mass flow, which are governed by the surface Navier–Stokes equation [9]. The necessity of addressing these coupled phenomena numerically serves as motivation for the development of adaptive surface FEMs with both first and second-order polynomial accuracy.

In this paper, our focus is on adaptive strategies for the stabilized TraceFEM applied to the Laplace–Beltrami equation, which serves as a prototypical elliptic problem on a surface Γ [10]. An overview of the motivation and the main results follow. At this point, we will omit certain technical details regarding the geometrical consistency of the adaptive method. To begin, consider an abstract variational problem on a surface Γ : given $f \in H^{-1}(\Gamma)$, we seek to find $u \in H^1(\Gamma)$ such that $a(u, v) = \langle f, v \rangle$ for all $v \in H^1(\Gamma)$. We assume that the bilinear form a is symmetric and coercive. In the TraceFEM, the discrete space V_h is defined on a graded, regular bulk mesh Ω_h , and we solve the following discrete problem:

$$a(u_h, v_h) + s_h(u_h, v_h) = \langle f, v_h \rangle, \quad \forall v_h \in V_h \quad (1)$$

Here, a stabilization form s_h ensures the algebraic stability of the resulting linear algebraic system. Residual and jump indicators can be derived [11] from the integration by parts in $a(u_h, v_h)$, as done in [4] for an unstabilized TraceFEM. However, in our case, the stabilization s_h is incorporated into an a posteriori estimate.

We would like to highlight two important aspects of the adaptivity methodology for the method (1):

- The jump indicator requires the construction of non-standard one-dimensional quadratures to handle curved intersections of the surface with faces of bulk cells. The associated implementation burden represents a practical inconvenience of the adaptive TraceFEM approach introduced in [4].
- We have observed that the ratio $s_h(u_h, u_h)/a(u_h, u_h)$, where both forms are restricted to a single bulk element, often exhibits significant growth, even for uniformly refined meshes. Consequently, the inclusion of the stabilization term s_h in an error indicator has the potential to compromise its efficiency.

To address the first aspect, we propose an alternative error indicator designed for adaptively refined, graded, octree tessellations of the bulk domain Ω , denoted as Ω_h . This novel indicator is reliable and straightforward to compute, as it eliminates the need for integration over the curved intersections of an implicitly defined surface with two-dimensional faces of the bulk cells. Instead, the indicator incorporates a jump term that only requires the use of a standard 2D quadrature for the faces of the bulk mesh cells. Moreover, for the TraceFEM stabilized with the gradient-jump face stabilization, this term is already an integral part of the method.

As for the second aspect, it is worth noting that the efficiency analysis of TraceFEM indicators remains an open question to the best of our knowledge. To explore this further, we undertake a comprehensive numerical investigation to assess the efficiency of the new indicator. In the case of stabilized TraceFEM with Q_1 finite elements, the indicator is found to be efficient. However, in the Q_2 case, efficiency gradually diminishes, although the convergence rates for the adaptive gradient-jump stabilized TraceFEM still appear to remain optimal.

The remainder of this paper is organized as follows: Section 2 introduces the stabilized adaptive TraceFEM along with a new computationally practical indicator. In Section 3, we provide a proof of the reliability estimate for the indicator. In Section 4, the adaptive method is tested numerically for low-regularity solutions to the Laplace–Beltrami equation on the unit sphere. We assess both the reliability and efficiency of the method, considering Q_1 and Q_2 conforming finite elements defined on octree meshes. Furthermore, we perform experiments using the adaptive TraceFEM with two different stabilizations.

2 The adaptive trace finite element method

We are interested in the geometrically unfitted finite element method known as the TraceFEM [12]. The method considered in this section is an extension of the TraceFEM and stabilization techniques introduced in [13, 14, 15] to hexahedral bulk octree meshes. After formulation of the method for our model problem, the Laplace–Beltrami equation, we introduce error indicators and an adaptive discretization.

2.1 Model problem

Let Ω be an open domain in \mathbb{R}^3 and let $\Gamma \subset \Omega$ be a smooth connected compact and closed hyper-surface embedded in \mathbb{R}^3 . For a sufficiently smooth function $g : \Omega \rightarrow \mathbb{R}$ the tangential derivative on Γ is defined by

$$\nabla_{\Gamma} g = \nabla g - (\nabla g \cdot \mathbf{n})\mathbf{n},$$

where \mathbf{n} denotes the unit normal to Γ . Denote by $\operatorname{div}_{\Gamma} = \operatorname{tr}(\nabla_{\Gamma})$ the surface divergence operator and by $\Delta_{\Gamma} = \nabla_{\Gamma} \cdot \nabla_{\Gamma}$ the Laplace–Beltrami operator on Γ . The Laplace–Beltrami equation is a model example of an elliptic PDE posed on the surface Γ . The equation reads as follows: find $u : \Gamma \rightarrow \mathbb{R}$ satisfying

$$-\Delta_{\Gamma} u + u = f \quad \text{on } \Gamma \quad (2)$$

The zero order term is added to avoid non-essential technical details of handling one-dimensional kernel consisting of all constant functions on Γ . The problem is well-posed in the sense of the weak formulation: Given $f \in H^{-1}(\Gamma)$, find $u \in H^1(\Gamma)$ satisfying

$$\int_{\Gamma} (\nabla_{\Gamma} u \cdot \nabla_{\Gamma} v + uv) ds = \int_{\Gamma} f v ds \quad \forall v \in H^1(\Gamma). \quad (3)$$

If $f \in L^2(\Gamma)$, then the unique solution satisfies $u \in H^2(\Gamma)$ and $\|u\|_{H^2(\Gamma)} \leq c\|f\|_{L^2(\Gamma)}$ with a constant c independent of f ; see [16].

2.2 Discretization

We assume an octree cubic mesh \mathcal{T}_h covering the bulk domain Ω . In addition, we assume that the mesh is *gradually* refined, i.e., the sizes of two active (finest level) neighboring cubes differ at most by a factor of 2. Such octree grids are also known as balanced. The method also applies for unbalanced octrees, but our analysis and experiments use balanced grids. The set of all active (finest level) faces is denoted by $\partial\mathcal{T}_h$. The mesh is not aligned with the surface Γ , which can cut through the cubes with no further restrictions.

By Γ_h we denote a given approximation of Γ such that Γ_h is a $C^{0,1}$ piecewise smooth surface without boundary and Γ_h is formed by smooth segments:

$$\Gamma_h = \bigcup_{T \in \mathcal{F}_h} \bar{T}, \quad (4)$$

where $\mathcal{F}_h = \{T \subset \Gamma_h : T = \Gamma_h \cap S, \text{ for } S \in \mathcal{T}_h\}$. For a given $T \in \mathcal{F}_h$ denote by S_T a cube $S_T \in \mathcal{T}_h$ such that $T \subset S_T$ (if T lies on a side shared by two cubes, any of these two cubes can be chosen as S_T).

In practice, we construct Γ_h as follows. Assume ϕ is a signed distance or general level set function for Γ . We define Γ_h as the zero level set of ϕ_h , a piecewise polynomial interpolant to ϕ on \mathcal{T}_h :

$$\Gamma_h := \{\mathbf{x} \in \Omega : \phi_h(\mathbf{x}) = 0\}.$$

For geometric consistency, the polynomial degree of ϕ_h is the same as the degree of piecewise polynomial functions we use to define trial and test spaces in a finite element formulation. In some applications, ϕ_h is recovered from a solution of a discrete indicator function equation (e.g. in the level set or the volume of fluid methods), without any direct knowledge of Γ . Assumptions of how well Γ_h should approximate Γ will be given later.

The unit (outward pointing) normal to Γ_h vector $\mathbf{n}_h = \nabla\phi_h/|\nabla\phi_h|$ is defined almost everywhere on Ω . We also define $\mathbf{P}_h(\mathbf{x}) := \mathbf{I} - \mathbf{n}_h(\mathbf{x})\mathbf{n}_h(\mathbf{x})^T$ for $\mathbf{x} \in \Gamma_h$, \mathbf{x} not on an edge. The tangential derivative along Γ_h is given by $\nabla_{\Gamma_h}g = \mathbf{P}_h\nabla g$ for sufficiently smooth g defined in a neighborhood of Γ_h .

Consider a subdomain ω_h of Ω consisting only of those end-level cubic cells that contain Γ_h :

$$\omega_h = \bigcup_{S \in \mathcal{T}_h^\Gamma} S, \quad \text{with } \mathcal{T}_h^\Gamma = \{S \in \mathcal{T}_h : S = S_T \text{ for } T \in \mathcal{F}_h\}. \quad (5)$$

The piecewise constant function $h_S : \omega_h \rightarrow \mathbb{R}$ denotes the bulk cubic cell size. Denote by Σ_h the set of all end-level internal faces of \mathcal{T}_h^Γ , i.e. square faces between intersected cells from \mathcal{T}_h^Γ ,

$$\Sigma_h = \{F \in \partial\mathcal{T}_h : F \in \text{int}(\omega_h)\}. \quad (6)$$

The piecewise constant function $h_F : \Sigma_h \rightarrow \mathbb{R}$ denotes the face size. Since the mesh is gradually refined, $h_F = \min(h_{S_F^+}, h_{S_F^-})$, where $S_F^+, S_F^- \in \mathcal{T}_h^\Gamma$ are the two bulk cells which share the end-level face $F \in \Sigma_h$.

We are also interested in the set of all faces which are intersected by Γ_h ,

$$\Sigma_h^\Gamma = \{F \in \Sigma_h : F \cap \Gamma_h \neq \emptyset\}. \quad (7)$$

Intersected faces are necessary internal, so that $\Sigma_h^\Gamma \subset \Sigma_h$, but the opposite inclusion does not hold.

For each cell S , let M_S be the affine mapping from the reference unit cube. Then the finite element space of order k is defined as :

$$V_h^k := \{v \in C(\omega_h) \mid v|_S \circ M_S \in Q_k, \forall S \in \mathcal{T}_h^\Gamma\}, \quad (8)$$

where Q_k is the Lagrangian finite element basis of degree k . In case of $k = 1$, $V_h = V_h^1$ is the space of piecewise trilinear functions corresponding to the family

$$Q_1 = \text{span}\{1, x_1, x_2, x_3, x_1x_2, x_1x_3, x_2x_3, x_1x_2x_3\}. \quad (9)$$

Note that we consider H^1 -conforming (i.e., continuous) finite elements. In this paper we restrict to $k = 1, 2$.

Let f^e be an extension of f from Γ to Γ_h . The finite element formulation reads: Find $u_h \in V_h^k$ such that

$$\int_{\Gamma_h} (\nabla_{\Gamma_h} u_h \cdot \nabla_{\Gamma_h} v_h + u_h v_h) ds + s_h(u_h, v_h) = \int_{\Gamma_h} f^e v_h ds \quad \forall v_h \in V_h^k. \quad (10)$$

Here s_h is a stabilization term defined later. The purpose of the stabilization term is to enhance the robustness of the formulation with respect to position of the position of Γ_h in the background mesh \mathcal{T}_h . In the context of TraceFEM the idea of stabilization was first introduced in [13].

2.3 TraceFEM stabilizations

We are interested in the two commonly used variants of the stabilization terms s_h in (10). In both cases, the stabilizing term can be assembled elementwise over all end-level cubes intersected by Γ_h :

$$s_h(u_h, v_h) = \sum_{S \in \mathcal{T}_h^\Gamma} s_S^*(u_h, v_h), \quad * \in \{JF, JF2, NV\}$$

1. **Gradient-jump face stabilization** is the method introduced in [13] following the cutFEM approach developed for the volumetric problems. In the context of the TraceFEM, this stabilization is often used with quasi-uniform bulk meshes, stationary surfaces, and lowest order elements; see e.g. [17, 18, 14, 15].

In this variant, local stabilizing terms are computed over cube's faces which are in the active skeleton (6),

$$s_S^{JF}(u_h, v_h) = \sum_{F \in \partial S \cap \Sigma_h} \int_F \sigma_F \llbracket \nabla u_h \rrbracket \cdot \llbracket \nabla v_h \rrbracket \quad (11)$$

where σ_F is $O(1)$ stabilization parameter, and $[[\nabla u_h]] = (\nabla u_h)|_{S^+} - (\nabla u_h)|_{S^-}$, $F = S^- \cap S^+$, is a “jump” of the gradient across the face. Note that for continuous FE, stabilization (11) is equivalent to penalizing the jumps of normal derivatives across faces.

A higher-order version of s_h^{JF} was suggested in [19] and analyzed for quasi-uniform meshes in [3]. For Q_2 elements it reads:

$$\begin{aligned} s_S^{JF^2}(u_h, v_h) &= s_S^{JF}(u_h, v_h) + \int_{\Gamma_h \cap S} \sigma_\Gamma (\mathbf{n}_h \cdot \nabla u_h)(\mathbf{n}_h \cdot \nabla v_h) \\ &+ \sum_{F \in \partial S \cap \Sigma_h} \int_F \tilde{\sigma}_F h_F^2 (\mathbf{n}_F \cdot [[\nabla^2 u_h]] \mathbf{n}_F)(\mathbf{n}_F \cdot [[\nabla^2 v_h]] \mathbf{n}_F) \\ &+ \int_{\Gamma_h \cap S} \tilde{\sigma}_\Gamma h_S^2 (\mathbf{n}_h \cdot (\nabla^2 u_h) \mathbf{n}_h)(\mathbf{n}_h \cdot (\nabla^2 v_h) \mathbf{n}_h), \end{aligned} \quad (12)$$

where σ_Γ , $\tilde{\sigma}_F$, and $\tilde{\sigma}_\Gamma$ are $O(1)$ tuning parameter. The bilinear form $s_h^{JF^2}$ stabilizes the trace finite element space V_h^2 in the case Q_2 polynomial family as shown in [3]. In that paper, a more general stabilization $h^\gamma s_h^{JF^2}$, $0 \leq \gamma \leq 2$, was considered and the sensitivity of the method to all stabilization parameters was explored. In our numerical results for Q_2 family, we choose $\sigma_F = \tilde{\sigma}_F = \tilde{\sigma}_\Gamma = \sigma_\Gamma$.

We see that the gradient-jump stabilization gets quite complicated for higher order elements. Below we consider a normal-gradient volume stabilization, which is universal with respect to the FE degree.

- 2. Normal-gradient volume stabilization** was introduced in [14, 15] and it penalizes the variation of the FE solution in the normal direction to the surface. This property was found particularly useful for applying TraceFEM to problems posed on evolving surfaces [20] and so it is commonly used in this context [21, 22, 23, 24]. The stabilization reads:

$$s_S^{NV}(u_h, v_h) = \int_S \rho_S (\mathbf{n}_h \cdot \nabla u_h)(\mathbf{n}_h \cdot \nabla v_h), \quad (13)$$

where ρ_S is the stabilization parameter, constant in each cell such that

$$\rho_S \simeq h_S^{-1} \quad \text{for } S \in \mathcal{T}_h^\Gamma.$$

Note that $\mathbf{n}_h = \nabla \phi_h / |\nabla \phi_h|$ is well-defined on ω_h so the integral in (13) makes sense.

2.4 Error indicators

One of the goals of this paper is to construct a new TraceFEM error estimator which does not involve complicated and expensive computations on edges $\Gamma_h \cap F$, $F \in \Sigma_h^\Gamma$. These edges are available only implicitly as intersections of Γ_h with bulk faces. Moreover, one needs to construct an immersed edge quadrature on each intersected face from Σ_h^Γ which is a significant computational burden. Again, note that some of the faces from Σ_h^Γ are subfaces of bulk cells which complicates the accumulation of flux jumps even further.

To this end, we define the *bulk jump* indicator:

$$\eta_F(S_T) = \|[[\nabla u_h]]\|_{L^2(\partial S_T \cap \omega_h)}, \quad S_T \in \mathcal{T}_h^\Gamma. \quad (14)$$

Note that the indicator (14) assesses the variation of the solution gradient across internal, square faces shared by the cubic cells in \mathcal{T}_h^Γ rather than across the implicit edges $\Gamma_h \cap F$, $F \in \Sigma_h^\Gamma$, as done in [25, 4, 5]. The former is more straightforward to compute. Also note that (14) is accumulated over all faces from (6) rather than just the intersected faces from (7).

We will also need the *surface residual* indicator,

$$\eta_R(T) = h_{S_T} \|f_h + \Delta_{\Gamma_h} u_h - u_h\|_{L^2(T)} \quad (15)$$

which was already used in [25, 4, 5]. The computation of the (15) requires integration over surface cuts $T = \Gamma_h \cap S_T$, $S_T \in \mathcal{T}_h^\Gamma$ which is a standard procedure in the implementation of TraceFEM (10).

Thus, for the purpose of local mesh adaptation we use the following error indicator:

$$\eta(S_T) := (\alpha_r \eta_R(T)^2 + \alpha_e \eta_F(S_T)^2 + \alpha_s s_{S_T}^*(u_h, u_h))^{\frac{1}{2}}. \quad (16)$$

with some parameters $\alpha_r, \alpha_e, \alpha_s \geq 0$.

Remark 2.1. Note that for the gradient-jump face stabilization, the solution's jumps over faces (i.e. the $\eta_F(S_T)^2$ quantity) are included in $s_{S_T}^*(u_h, u_h)$ term and so the face indicator is extra and we let $\alpha_e = 0$ in the cases of Q_1 and Q_2 . Otherwise, in our numerical experiments with normal-gradient volume, we choose $\alpha_r = \alpha_e = \alpha_s = 1$.

In this paper we do not consider any indicator of the geometric error resulting from the approximation Γ and other geometric quantities. They are assumed to be of a higher order with respect to h_S .

Results of experiments in Section 4 show that the trace FE adaptive method based on $\eta(T)$ results in the optimal convergence of the adaptive method in H^1 and L^2 norms.

3 Reliability

In this section we prove an a posteriori error estimate that implies the reliability the error indicator (16). We start with several preliminaries.

3.1 Preliminaries

For the surface Γ , we consider its neighborhood:

$$\mathcal{O}(\Gamma) := \{\mathbf{x} \in \mathbb{R}^3 \mid \text{dist}(\mathbf{x}, \Gamma) < \tilde{c}\}, \quad (17)$$

with a suitable \tilde{c} depending on Γ such that $\omega_h \subset \mathcal{O}(\Gamma) \subset \Omega$ and the normal projection $\mathbf{p} : \mathcal{O}(\Gamma) \rightarrow \Gamma$,

$$\mathbf{p}(\mathbf{x}) = \mathbf{x} - d(\mathbf{x})\mathbf{n}(\mathbf{x})$$

is well-defined. Hereafter $d \in C^2(\mathcal{O}(\Gamma))$ denotes the signed distance function such that $d < 0$ in the interior of Γ and $d > 0$ in the exterior, and $\mathbf{n}(\mathbf{x}) := \nabla d(\mathbf{x})$ for all $\mathbf{x} \in \mathcal{O}(\Gamma)$. Hence, \mathbf{n} is the normal vector on Γ and $|\mathbf{n}(\mathbf{x})| = 1$ for all $\mathbf{x} \in \mathcal{O}(\Gamma)$. The Hessian of d is denoted by

$$\mathbf{H}(\mathbf{x}) := \nabla^2 d(\mathbf{x}) \in \mathbb{R}^{3 \times 3}, \quad \mathbf{x} \in \mathcal{O}(\Gamma).$$

The eigenvalues of $\mathbf{H}(\mathbf{x})$ are the principal curvatures $\kappa_1(\mathbf{x})$, $\kappa_2(\mathbf{x})$, and 0.

We assume the following estimates on how well Γ_h approximates Γ :

$$\text{ess sup}_{\mathbf{x} \in \Gamma_h} |d(\mathbf{x})| \leq c_1 h^{k+1}, \quad (18)$$

$$\text{ess sup}_{\mathbf{x} \in \Gamma_h} |\mathbf{n}(\mathbf{x}) - \mathbf{n}_h(\mathbf{x})| \leq c_2 h^k, \quad (19)$$

with constants c_1, c_2 independent of h and $k \in \{1, 2\}$ in the FE degree. The assumption is reasonable if Γ is defined as the zero level of a (locally) smooth level set function ϕ and Γ_h is the zero of an $\phi_h \in V_h$, where ϕ_h interpolates ϕ and it holds

$$\|\phi - \phi_h\|_{L^\infty(\mathcal{O}(\Gamma))} + h \|\nabla(\phi - \phi_h)\|_{L^\infty(\mathcal{O}(\Gamma))} \lesssim h^{k+1}.$$

Here and in the remainder, $A \lesssim B$ means $A \leq cB$ for some positive constant c independent of the number of refinement levels and the position of Γ_h in the background mesh.

For $\mathbf{x} \in \Gamma_h$, define $\mu_h(\Gamma)(\mathbf{x}) = (1 - d(\mathbf{x})\kappa_1(\mathbf{x}))(1 - d(\mathbf{x})\kappa_2(\mathbf{x}))\mathbf{n}^T(\mathbf{x})\mathbf{n}_h(\mathbf{x})$. The surface measures ds and ds_h on Γ and Γ_h , respectively, are related [25] by

$$\mu_h(\Gamma)(\mathbf{x}) ds_h(\mathbf{x}) = ds(\mathbf{p}(\mathbf{x})), \quad \mathbf{x} \in \Gamma_h. \quad (20)$$

The solution of the Laplace–Beltrami problem and its data are defined on Γ , while the finite element method is defined on Γ_h . Hence, we need a suitable extension of a function from Γ to its neighborhood. For a function v on Γ we define

$$v^e(\mathbf{x}) := v(\mathbf{p}(\mathbf{x})) \quad \text{for all } \mathbf{x} \in \mathcal{O}(\Gamma).$$

The following formulas for this extended function are well-known (cf. section 2.3 in [25]):

$$\nabla u^e(\mathbf{x}) = (\mathbf{I} - d(\mathbf{x})\mathbf{H})\nabla_{\Gamma}u(\mathbf{p}(\mathbf{x})) \quad \text{in } \mathcal{O}(\Gamma), \quad (21)$$

$$\nabla_{\Gamma_h}u^e(\mathbf{x}) = \mathbf{P}_h(\mathbf{x})(\mathbf{I} - d(\mathbf{x})\mathbf{H})\nabla_{\Gamma}u(\mathbf{p}(\mathbf{x})) \quad \text{a.e. on } \Gamma_h, \quad (22)$$

with $\mathbf{H} = \mathbf{H}(\mathbf{x})$. For $\mathbf{x} \in \Gamma_h$ also define $\tilde{\mathbf{P}}_h(\mathbf{x}) = \mathbf{I} - \mathbf{n}_h(\mathbf{x})\mathbf{n}(\mathbf{x})^T/(\mathbf{n}_h(\mathbf{x}) \cdot \mathbf{n}(\mathbf{x}))$. One can represent the surface gradient of $u \in H^1(\Gamma)$ in terms of $\nabla_{\Gamma_h}u^e$ as follows

$$\nabla_{\Gamma}u(\mathbf{p}(\mathbf{x})) = (\mathbf{I} - d(\mathbf{x})\mathbf{H}(\mathbf{x}))^{-1}\tilde{\mathbf{P}}_h(\mathbf{x})\nabla_{\Gamma_h}u^e(\mathbf{x}) \quad \text{a.e. } \mathbf{x} \in \Gamma_h. \quad (23)$$

Due to (20) and (23), one gets

$$\int_{\Gamma} \nabla_{\Gamma}u \nabla_{\Gamma}v \, ds = \int_{\Gamma_h} \mathbf{A}_h \nabla_{\Gamma_h}u^e \nabla_{\Gamma_h}v^e \, ds_h \quad \text{for all } v \in H^1(\Gamma), \quad (24)$$

with $\mathbf{A}_h(\mathbf{x}) = \mu_h(\mathbf{x})\tilde{\mathbf{P}}_h^T(\mathbf{x})(\mathbf{I} - d(\mathbf{x})\mathbf{H}(\mathbf{x}))^{-2}\tilde{\mathbf{P}}_h(\mathbf{x})$.

For sufficiently smooth u and $|\mu| \leq 2$, it holds (cf. Lemma 3 in [10]):

$$|D^{\mu}u^e(\mathbf{x})| \lesssim \left(\sum_{|\mu|=2} |D_{\Gamma}^{\mu}u(\mathbf{p}(\mathbf{x}))| + |\nabla_{\Gamma}u(\mathbf{p}(\mathbf{x}))| \right) \quad \text{in } \mathcal{O}(\Gamma), \quad (25)$$

We need the following uniform trace inequalities. For any end level cell $S \subset \omega_h$ and its face $F \subset S$ it holds

$$\|v\|_{L^2(S \cap \Gamma_h)}^2 \lesssim h_S^{-1}\|v\|_{L^2(S)}^2 + h_S\|\nabla v\|_{L^2(S)}^2 \quad \forall v \in H^1(S). \quad (26)$$

$$\|v\|_{L^2(F \cap \Gamma_h)}^2 \lesssim h_F^{-1}\|v\|_{L^2(F)}^2 + h_F\|\nabla v\|_{L^2(F)}^2 \quad \forall v \in H^1(F). \quad (27)$$

Note that for graded octree meshes it holds $h_F \simeq h_S$. The proof of (26) follows by subdividing any cubic cell into a finite number of regular tetrahedra and further applying Lemma 4.2 from [26] on each of these tetrahedra. Similar procedure is applied to prove (27).

We will use the following notation

$$a_h(u, v) := \int_{\Gamma_h} (\nabla_{\Gamma_h}u \cdot \nabla_{\Gamma_h}v + uv) \, ds_h.$$

3.2 A posteriori estimate

In this section, we deduce an a posteriori error estimate for the TraceFEM (10). For the sake of analysis we make the following *assumptions*:

- (i) The octree mesh is gradually refined;
- (ii) For any $\mathbf{s} \in \Gamma$ denote by $K(\mathbf{s})$ a number of end-level cubic cells from ω_h intersected by the line $\ell(\mathbf{s}) = \{\mathbf{x} \in \mathcal{O}(\Gamma) : \mathbf{p}(\mathbf{x}) = \mathbf{s}\}$. We assume $K(\mathbf{s}) \leq K$ with a constant K independent of \mathbf{s} and the number of refinement levels.

In practice, the first assumption can be satisfied by triggering the refinement of any cell which has a finer neighbor already marked for refinement. The second assumption does not pose any practical restrictions and in experiments we observed that $K(\mathbf{s})$ is small for all \mathbf{s} sampled for testing. An explanation of why Assumption (ii) is reasonable relies on the smoothness of Γ and the use of gradually refined meshes. Indeed

for a C^2 surface, one can choose such $O(1)$ neighborhood $\mathcal{O}(\Gamma)$ that $\ell(\mathbf{s})$ intersects Γ only once at point \mathbf{s} . Assume $K(\mathbf{s}) \rightarrow \infty$ with a mesh refinement for some $\mathbf{s} \in \Gamma$. Since the end-level cells are getting arbitrary small, this implies that $\ell(\mathbf{s})$ intersects or touches Γ at the point of accumulation. However, such only point can be \mathbf{s} and $\ell(\mathbf{s}) \perp \Gamma(\mathbf{s})$ while Γ is increasingly flat in the local (mesh) scale. For a graded mesh, this may result only in a finite number of intersected end-level cells.

Consider the surface finite element error $e_h = u^e - u_h$ in ω_h . By e_h^l we denote the lift of the error function on $\mathcal{O}(\Gamma)$, $e_h^l(\mathbf{x}) = u(\mathbf{p}(\mathbf{x})) - u_h(\mathbf{s})$ with $\mathbf{s} \in \Gamma_h$ such that $\mathbf{p}(\mathbf{s}) = \mathbf{p}(\mathbf{x})$. Note that e_h^l is constant in normal directions to Γ , i.e. $e_h^l = (e_h^l|_\Gamma)^e$. Further we prove an a posteriori bound for the augmented H^1 -norm of e_h^l on Γ , i.e. for

$$\|e_h\|^2 = a(e_h^l, e_h^l) + s_h(e_h, e_h), \quad \text{with } a(u, v) = \int_\Gamma (\nabla_\Gamma u \cdot \nabla_\Gamma v + uv) ds. \quad (28)$$

Using straightforward calculations and (24) one checks the following identities for any $\psi_h \in V_h$

$$\begin{aligned} \|e_h\|^2 &= \int_\Gamma f e_h^l ds - a(u_h^l, e_h^l) + s_h(e_h, e_h) \\ &= \int_{\Gamma_h} f^e e_h \mu_h ds_h - \int_{\Gamma_h} f_h \psi_h ds_h + a_h(u_h, \psi_h) + s_h(u_h, \psi_h) - a(u_h^l, e_h^l) + s_h(e_h, e_h) \\ &= \int_{\Gamma_h} (f^e \mu_h - f_h) e_h ds_h + \int_{\Gamma_h} f_h (e_h - \psi_h) ds_h + a_h(u_h, \psi_h - e_h) + s_h(u_h, \psi_h - e_h) \\ &\quad - \int_{\Gamma_h} (\mathbf{A}_h - \mathbf{P}_h) \nabla_{\Gamma_h} u_h \cdot \nabla_{\Gamma_h} e_h ds_h. \end{aligned} \quad (29)$$

Element-wise integration by parts for the third term on the right hand side of (29) gives

$$a_h(u_h, \psi_h - e_h) = \int_{\Gamma_h} (\Delta_{\Gamma_h} u_h - u_h)(e_h - \psi_h) ds_h - \frac{1}{2} \sum_{T \in \mathcal{F}_h} \int_{\partial T} \llbracket \nabla_{\Gamma_h} u_h \rrbracket (e_h - \psi_h) dr. \quad (30)$$

The Cauchy inequality gives

$$s_h(u_h, \psi_h - e_h) \leq \left(\sum_{S \in \mathcal{T}_h^\Gamma} s_S^*(u_h, u_h) \right)^{\frac{1}{2}} \left(\sum_{S \in \mathcal{T}_h^\Gamma} s_S^*(\psi_h - e_h, \psi_h - e_h) \right)^{\frac{1}{2}}.$$

Substituting (30) into (29) and applying the Cauchy inequality elementwise over \mathcal{F}_h to estimate integrals, we get

$$\begin{aligned} \|e_h\|^2 &\lesssim \sum_{T \in \mathcal{F}_h} (\|f^e \mu_h - f_h\|_{L^2(T)} + \|\mathbf{A}_h - \mathbf{P}_h\|_{L^\infty(T)} \|\nabla_{\Gamma_h} u_h\|_{L^2(T)}) \|e_h\|_{H^1(\Gamma_h)} \\ &\quad + \left(\sum_{T \in \mathcal{F}_h} \eta_R(T)^2 \right)^{\frac{1}{2}} \left(\sum_{T \in \mathcal{F}_h} h_{S_T}^{-2} \|e_h - \psi_h\|_{L^2(T)}^2 \right)^{\frac{1}{2}} \\ &\quad + \left(\sum_{T \in \mathcal{F}_h} h_{S_T} \|\llbracket \nabla_{\Gamma_h} u_h \rrbracket\|_{\partial T}^2 \right)^{\frac{1}{2}} \left(\sum_{T \in \mathcal{F}_h} h_{S_T}^{-1} \|e_h - \psi_h\|_{L^2(\partial T)}^2 \right)^{\frac{1}{2}} \\ &\quad + \left(\sum_{S \in \mathcal{T}_h^\Gamma} s_S^*(u_h, u_h) \right)^{\frac{1}{2}} \left(\sum_{S \in \mathcal{T}_h^\Gamma} s_S^*(\psi_h - e_h, \psi_h - e_h) \right)^{\frac{1}{2}}. \end{aligned} \quad (31)$$

To proceed further we need several results, which we split into a few lemmas.

Lemma 3.1. *For all $T \in \mathcal{F}_h$ it holds*

$$h_{S_T} \|\llbracket \nabla_{\Gamma_h} u_h \rrbracket\|_{L^2(\partial T)}^2 \lesssim \eta_F(S_T)^2. \quad (32)$$

Proof. Recall that the face-based indicator $\eta_F(S_T)$ for a cell S_T includes all internal faces $F \in \partial S_T \cap \Sigma_h$ rather than only faces from $\partial S_T \cap \Sigma_h^\Gamma$. Also note that $\llbracket \nabla_{\Gamma_h} u_h \rrbracket = \llbracket \mathbf{P}_h \nabla u_h \rrbracket$ is a rational function of a finite degree on each face of S_T . Application of the uniform trace estimate (27) followed by the FE inverse estimate on each face $F \subset \partial S_T \cap \Sigma_h^\Gamma$ gives the assertion. \square

Lemma 3.2. *The following bound holds for both stabilizations and FE degrees:*

$$s_S^*(\psi_h - e_h, \psi_h - e_h) \lesssim s_S^*(e_h, e_h) + h_S^{-1} \|\nabla \psi_h\|_{L^2(\omega(S))}^2. \quad (33)$$

where $\omega(S)$ denotes a union of cubic cells from ω_h sharing faces with S .

Proof. We first apply the triangle inequality to show

$$s_S^*(\psi_h - e_h, \psi_h - e_h) \leq 2(s_S^*(e_h, e_h) + s_S^*(\psi_h, \psi_h)) \quad (34)$$

We need to estimate the second term on the right-hand side. For the gradient-jump stabilization and $k = 2$ we have

$$\begin{aligned} s_S^{JF2}(\psi_h, \psi_h) &= \sigma_\Gamma \|\mathbf{n}_h \cdot \nabla \psi_h\|_{L^2(\Gamma_h \cap S)}^2 + \tilde{\sigma}_\Gamma h_S^2 \|\mathbf{n}_h \cdot (\nabla^2 \psi_h) \mathbf{n}_h\|_{L^2(\Gamma_h \cap S)}^2 \\ &\quad + \sum_{F \in \partial S \cap \Sigma_h} \left(\sigma_F \|\llbracket \nabla \psi_h \rrbracket\|_{L^2(F)}^2 + \tilde{\sigma}_F h_F^2 \|\mathbf{n}_F \cdot \llbracket \nabla^2 \psi_h \rrbracket \mathbf{n}_F\|_{L^2(F)}^2 \right). \end{aligned} \quad (35)$$

To estimate the first two terms on the right-hand side of (35), we apply the trace estimate (26):

$$\begin{aligned} \|\mathbf{n}_h \cdot \nabla \psi_h\|_{L^2(\Gamma_h \cap S)}^2 &\leq \|\nabla \psi_h\|_{L^2(\Gamma_h \cap S)}^2 \lesssim h_S^{-1} \|\nabla \psi_h\|_{L^2(S)}^2 + h_S \|\nabla^2 \psi_h\|_{L^2(S)}^2 \lesssim h_S^{-1} \|\nabla \psi_h\|_{L^2(S)}^2 \\ h_S^2 \|\mathbf{n}_h \cdot (\nabla^2 \psi_h) \mathbf{n}_h\|_{L^2(\Gamma_h \cap S)}^2 &\leq h_S^2 \|\nabla^2 \psi_h\|_{L^2(\Gamma_h \cap S)}^2 \lesssim h_S \|\nabla^2 \psi_h\|_{L^2(S)}^2 \lesssim h_S^{-1} \|\nabla \psi_h\|_{L^2(S)}^2. \end{aligned} \quad (36)$$

To estimate the third and fourth terms on the right-hand side of (35), we apply the finite element trace and inverse inequalities:

$$\begin{aligned} \sum_{F \in \partial S \cap \Sigma_h} \sigma_F \|\llbracket \nabla \psi_h \rrbracket\|_{L^2(F)}^2 &\lesssim \|\llbracket \nabla \psi_h \rrbracket\|_{L^2(\partial S \cap \Sigma_h)}^2 \lesssim h_S^{-1} \|\nabla \psi_h\|_{L^2(\omega(S))}^2 \\ \sum_{F \in \partial S \cap \Sigma_h} h_F^2 \|\mathbf{n}_F \cdot \llbracket \nabla^2 \psi_h \rrbracket \mathbf{n}_F\|_{L^2(F)}^2 &\lesssim h_S^2 \|\llbracket \nabla^2 \psi_h \rrbracket\|_{L^2(\partial S \cap \Sigma_h)}^2 \lesssim h_S \|\nabla^2 \psi_h\|_{L^2(\omega(S))}^2 \\ &\lesssim h_S^{-1} \|\nabla \psi_h\|_{L^2(\omega(S))}^2. \end{aligned} \quad (37)$$

The combination of (35)–(37) gives

$$s_S^{JF2}(\psi_h, \psi_h) \lesssim h_S^{-1} \|\nabla \psi_h\|_{L^2(\omega(S))}^2. \quad (38)$$

Of course, the same bound (38) holds also for $k = 1$. For the normal-volume stabilization we have

$$s_S^{NV}(\psi_h, \psi_h) = \rho_S \|\mathbf{n}_h \cdot \nabla \psi_h\|_{L^2(S)}^2 \lesssim h_S^{-1} \|\mathbf{n}_h \cdot \nabla \psi_h\|_{L^2(S)}^2, \quad (39)$$

where we used that ρ_S is an $O(h_S^{-1})$ parameter. Substituting (38) and (39) in (34) proves the lemma. \square

Due to geometric approximation properties (18), (19) and “lifting” identities (20) and (22) we have

$$\|e_h\|_{H^1(\Gamma_h)} \lesssim \|e_h^l\|_{H^1(\Gamma)}. \quad (40)$$

Lemma 3.3. *There exist $\psi_h \in V_h$ such that*

$$\sum_{T \in \mathcal{F}_h} \left[h_{S_T}^{-2} \|e_h - \psi_h\|_{L^2(T)}^2 + h_{S_T}^{-1} \|e_h - \psi_h\|_{L^2(\partial T)}^2 + s_S^*(\psi_h - e_h, \psi_h - e_h) \right] \lesssim \|e_h\|^2. \quad (41)$$

Proof. To handle the edge term on the left-hand side of (41), we need some further constructions: For a curved edge $e \subset \partial T$ denote by $F_e \subset \partial S_T$ the face of S_T such that $e \subset F_e$. Denote by $\omega(e) \subset \mathcal{T}_h$ the set of all cubic cells touching F_e . Let $\tilde{\phi}_h$ be the natural polynomial extension of the level-set function $\phi_h|_{S_T}$ and $\tilde{\Gamma}_h(e) = \{\mathbf{x} \in \omega(e) : \tilde{\phi}_h(\mathbf{x}) = 0\}$ be a smooth approximation of Γ locally in $\omega(e)$. Note that due to the graded refinement assumption there is a $h_{S_T}/2$ neighborhood of e in $\tilde{\Gamma}_h(e)$. Then for $\rho \in H^1(\tilde{\Gamma}_h(e))$ in holds

$$\|\rho\|_{L^2(e)}^2 \lesssim h_{S_T}^{-1} \|\rho\|_{L^2(\tilde{\Gamma}_h(e))}^2 + h_{S_T} \|\nabla_{\tilde{\Gamma}_h(e)} \rho\|_{L^2(\tilde{\Gamma}_h(e))}^2. \quad (42)$$

The estimate (42) follows from a standard flattening argument and applying a trace inequality as in (27).

We apply the bulk and (26) trace inequalities and (42) to estimate

$$\begin{aligned} & h_{S_T}^{-2} \|e_h - \psi_h\|_{L^2(T)}^2 + \sum_{e \in \partial T} h_{S_T}^{-1} \|e_h - \psi_h\|_{L^2(e)}^2 \\ & \lesssim h_{S_T}^{-3} \|e_h^l - \psi_h\|_{L^2(S_T)}^2 + h_{S_T}^{-1} \|\nabla(e_h^l - \psi_h)\|_{L^2(S_T)}^2 \\ & \quad + \sum_{e \in \partial T} \left(h_{S_T}^{-2} \|e_h^l - \psi_h\|_{L^2(\tilde{\Gamma}_h(e))}^2 + \|\nabla_{\tilde{\Gamma}_h}(e_h^l - \psi_h)\|_{L^2(\tilde{\Gamma}_h(e))}^2 \right) \\ & \lesssim h_{S_T}^{-3} \|e_h^l - \psi_h\|_{L^2(\omega(e))}^2 + h_{S_T}^{-1} \|\nabla(e_h^l - \psi_h)\|_{L^2(\omega(e))}^2 \\ & \quad + \sum_{e \in \partial T} \left(\|\nabla_{\tilde{\Gamma}_h} e_h^l\|_{L^2(\tilde{\Gamma}_h(e))}^2 + \|\nabla \psi_h\|_{L^2(\tilde{\Gamma}_h(e))}^2 \right) \\ & \lesssim h_{S_T}^{-3} \|e_h^l - \psi_h\|_{L^2(\omega(e))}^2 + h_{S_T}^{-1} \|\nabla(e_h^l - \psi_h)\|_{L^2(\omega(e))}^2 \\ & \quad + \sum_{e \in \partial T} \left(\|\nabla_{\Gamma} e_h^l\|_{L^2(\mathbf{p}(\tilde{\Gamma}_h(e)))}^2 + h_{S_T}^{-1} \|\nabla \psi_h\|_{L^2(\omega(e))}^2 \right), \end{aligned} \quad (43)$$

where we used an estimate

$$\|\nabla_{\tilde{\Gamma}_h} e_h^l\|_{L^2(\tilde{\Gamma}_h(e))} \lesssim \|\nabla_{\Gamma} e_h^l\|_{L^2(\mathbf{p}(\tilde{\Gamma}_h(e)))}, \quad (44)$$

which holds due to (20), (22) and the fact that (18), (19) also hold for the locally extended Γ_h with possibly different $O(1)$ constants c_1, c_2 . Also note that for any lifted function $u^l \in L^2(\omega_h)$

$$\|u^l\|_{L^2(S)}^2 \lesssim h_{S_T} \|u^l\|_{L^2(\mathbf{p}(S))}^2. \quad (45)$$

Thanks to our assumption (i) there is a Scott-Zhang type interpolant $\psi_h \in V_h$ of $e_h^l \in H^1(\Omega)$ [27] such that

$$h_S^{-1} \|e_h^l - \psi_h\|_{L^2(S)} + \|\nabla \psi_h\|_{L^2(S)} \lesssim \|e_h^l\|_{H^1(\omega(S))} \quad \forall S \in \Omega_h, \quad (46)$$

where $\omega(S)$ is defined as follows: Let $\tilde{\omega}(S)$ consist of S and of all end-level cubic cells touching S , then $\omega(S)$ is a patch of cells defined as the union of $\tilde{\omega}(S)$ and of all end-level cubic cells touching $\tilde{\omega}(S)$. We assume \tilde{c} in (17) to be sufficiently large and h sufficiently small that $\omega(S) \subset \mathcal{O}(\Gamma)$ for all $S \in \Omega_h$.

Applying in (43) the estimates from (46), (45) and the result from Lemma 3.1 yields

$$\begin{aligned} & \sum_{T \in \mathcal{F}_h} \left[h_{S_T}^{-2} \|e_h - \psi_h\|_{L^2(T)}^2 + h_{S_T}^{-1} \|e_h - \psi_h\|_{L^2(\partial T)}^2 + s_{S_T}^* (\psi_h - e_h, \psi_h - e_h) \right] \\ & \lesssim \sum_{T \in \mathcal{F}_h} \left(h_{S_T}^{-1} \|e_h^l\|_{H^1(\omega(S_T))}^2 + \|\nabla_{\Gamma} e_h^l\|_{L^2(\mathbf{p}(\omega(S_T)))}^2 + h_S^{-1} \|\nabla \psi_h\|_{L^2(\omega(S_T))}^2 \right) \\ & \lesssim \sum_{T \in \mathcal{F}_h} \left(h_{S_T}^{-1} \|e_h^l\|_{H^1(\omega(S_T))}^2 + \|\nabla_{\Gamma} e_h^l\|_{L^2(\mathbf{p}(\omega(S_T)))}^2 \right) \\ & \lesssim \sum_{S \in \omega_h} \|e_h^l\|_{H^1(\mathbf{p}(\omega(S_T)))}^2. \end{aligned} \quad (47)$$

In the last inequality we also used the fact that for the graded octree mesh $\text{diam}(\omega(S_T)) \simeq h_{S_T}$. Due to assumption (i) any cell S_T may belong to a uniformly bounded number of patches. Thanks to this and

assumption (ii) any $\mathbf{x} \in \Gamma$ may belong to the projections of patches which total number is also uniformly bounded. This establishes the bound

$$\sum_{T \in \mathcal{F}_h} \|e_h^l\|_{H^1(\mathbf{p}(\omega(S_T)))}^2 \lesssim \|e_h^l\|_{H^1(\Gamma)}^2. \quad (48)$$

Using (43)–(48) proves the lemma. \square

Combining (31), (32) and (40), (41) gives the following *a posteriori* error estimate

$$\|e_h\| \lesssim \left(\sum_{T \in \mathcal{F}_h} \|f^e \mu_h - f_h\|_{L^2(T)}^2 + \|\mathbf{A}_h - \mathbf{P}_h\|_{L^\infty(T)}^2 \|\nabla_{\Gamma_h} u_h\|_{L^2(T)}^2 \right)^{\frac{1}{2}} + \left(\sum_{T \in \mathcal{F}_h} [\eta_R(T)^2 + \eta_F(S_T)^2 + s_{S_T}^*(u_h, u_h)] \right)^{\frac{1}{2}}. \quad (49)$$

Assume that local grid refinement leads to better local surface reconstruction, i.e. (18) and (19) can be formulated locally, then it holds $\|f^e \mu_h - f_h\|_{L^2(T)} + \|\mathbf{A}_h - \mathbf{P}_h\|_{L^\infty(T)} = O(h^{k+1})$. In this case, the first term on the right-hand side of (49) is of higher order if $k \geq 1$ for Q_1 and $k \geq 2$ for Q_2 .

4 Numerical examples

This section presents a numerical study of an adaptive version of the stabilized TraceFEM (10), which relies on the novel indicator (49). First, we provide details of the adaptive algorithm, including the surface approximation, in Section 4.2. Next, we confirm *a posteriori* estimates for the families Q_1 and Q_2 . Moreover, we address the efficiency of the indicator using a manufactured solution. We test both gradient jump and normal gradient volume stabilizations. However, we omit the bulk jump indicator $\eta_F(S_T)$ (14) in the proposed indicator (53) if the TraceFEM scheme (52) is stabilized by including s_h^{JF} or s_h^{JF2} forms; see Remark 2.1.

4.1 A low-regularity test case

This section discusses the model problem (3), the solution of which is not regular enough to provide optimal rates of convergence if uniform refinement is employed. We consider the unit sphere Γ and a family of solutions $u = u_\lambda \in H^{1+\lambda}(\Gamma)$, $0 \leq \lambda \leq 1$, such that

$$-\Delta_\Gamma u + u = f, \quad (50)$$

with the forcing $f = f_\lambda \in H^{\lambda-1}(\Gamma)$. Consequently, by choosing different values of λ , we may obtain exact solutions of desired regularity. An example [5] of such a family is given in spherical polar coordinates (ϕ, θ) , $\theta \in [0, \pi]$, $\phi \in (-\pi, \pi]$, by

$$u = \sin^\lambda \theta \sin \phi, \quad f = (1 + \lambda^2 + \lambda) \sin^\lambda \theta \sin \phi + (1 - \lambda^2) \sin^{\lambda-2} \theta \sin \phi. \quad (51)$$

Clearly, u and f have singularities at the north, $\theta = 0$ or $(x, y, z) = (0, 0, 1)$, and the south, $\theta = \pi$ or $(x, y, z) = (0, 0, -1)$, poles (see Figure 1) while being harmonic in the azimuthal direction ϕ for each fixed $\theta \neq 0, \pi$.

Before the iterative adaptive procedure starts, one constructs a sufficiently fine mesh of $\Omega = [-2, 2]^3$ so the initial surface approximation Γ_h is well-defined. To this end, the distance function $d(x, y, z) = x^2 + y^2 + z^2 - 1$ is chosen for the level-set description of the unit sphere Γ . The edges of the cube Ω are divided in eight equal segments of length $h = 0.5$, see Figure 1, cycle=0. These cells constitute the initial mesh \mathcal{T}_h .

4.2 Adaptive stabilized TraceFEM

In this section we present the adaptive algorithm tested in the numerical experiments. The adaptive procedure is a sequence of cycles each consisting of the three steps below.

Step 1 (APPROXIMATE GEOMETRY). To guarantee continuity of the surface approximation, we first resolve all hanging nodes in \mathcal{T}_h by adding a sufficient number of linear constraints. The interpolant ϕ_h^k of order k of the distance function d on the mesh \mathcal{T}_h identifies the active domain ω_h consisting of intersected cells \mathcal{T}_h^Γ . Geometrical information such as the normal vector \mathbf{n}_h and the surface quadratures representing Γ_h is derived from the discrete distance function ϕ_h^k .

Step 2 (SOLVE). The finite element space V_h^k consists of continuous piece-wise Q_1 or Q_2 functions defined on \mathcal{T}_h^Γ . We solve the following linear system: find $u_h \in V_h^k$ such that

$$\int_{\Gamma_h} \nabla_{\Gamma_h} u_h \cdot \nabla_{\Gamma_h} v_h + \int_{\Gamma_h} u_h v_h + s_h(u_h, v_h) = (f^e, v_h)_{\Gamma_h}, \quad \forall v_h \in V_h^k \quad (52)$$

where the term s_h represents one of stabilizations from Section 2.3.

Step 3 (ESTIMATE&MARK&REFINE). Fix a $0 < \theta < 1$. Using the discrete solution u_h , we compute the indicator $\eta(S_T)$,

$$\eta^2(S_T) = \|\llbracket \nabla u_h \rrbracket\|_{L^2(\partial S_T \cap \omega_h)}^2 + h_{S_T}^2 \|f^e + \Delta_{\Gamma_h} u_h - u_h\|_{L^2(T)}^2 + s_{S_T}^*(u_h, u_h) \quad (53)$$

on each intersected cell $S_T \in \mathcal{T}_h^\Gamma$. Next we determine the smallest by cardinality set $\mathcal{T}_h^\theta \subset \mathcal{T}_h^\Gamma$ such that

$$\sum_{S_T \in \mathcal{T}_h^\theta} \eta^2(S_T) > \theta \sum_{S_T \in \mathcal{T}_h^\Gamma} \eta^2(S_T) \quad (54)$$

and, finally, refine the cells in \mathcal{T}_h^θ uniformly.

This completes the first cycle. At the beginning of the next cycle the new mesh \mathcal{T}_h , refined near Γ , of the domain Ω is available and we proceed to Step 1.

4.3 Unfitted quadratures and other implementation details

The adaptive stabilized TraceFEM scheme of Section 4.2 was implemented in the Finite Element library **deal.II** [28, 29]. Since the method is not standard, we start with discussing some implementation details.

- The degrees of freedom of the level-set function exist across the entire mesh domain, whereas the degrees of freedom of the solution are confined to the colored, active domain of intersected cells. In principle, the discrete level-set approximation could have a different order or even an independent mesh from that of the solution. However, for the sake of convenience, we utilized the same triangulation for both the solution and the level-set in our implementation.
- Given that the mesh contains hanging nodes, ensuring the continuity of the FE spaces defined on it is necessary for a H^1 -conforming method. This continuity requirement extends to both the discrete level-set and the discrete solution. To achieve this, we express the continuity condition for each hanging node as a linear combination involving local degrees of freedom, which is subsequently incorporated into the linear system. We apply a similar post-processing technique to the discrete level-set function, defined by a point-wise Lagrange interpolant, to eliminate any gaps in the discrete surface Γ_h .
- The implementation of (52) requires the integration of polynomial functions over the intersections of the implicit surface Γ_h with end cells from \mathcal{T}_h^Γ . This procedure is non-standard, and our implementation relies on the dimension-reduction approach detailed in [30]. Notably, this algorithm is purpose-built for quadrilaterals and can accommodate higher-order approximations of Γ_h .
- Implementation of stabilization forms s_h^{NV} and s_h^{JF} requires standard, e.g. Gauss–Lobatto, quadratures on a three-dimensional cube S_T and on a two-dimensional square F , correspondingly.

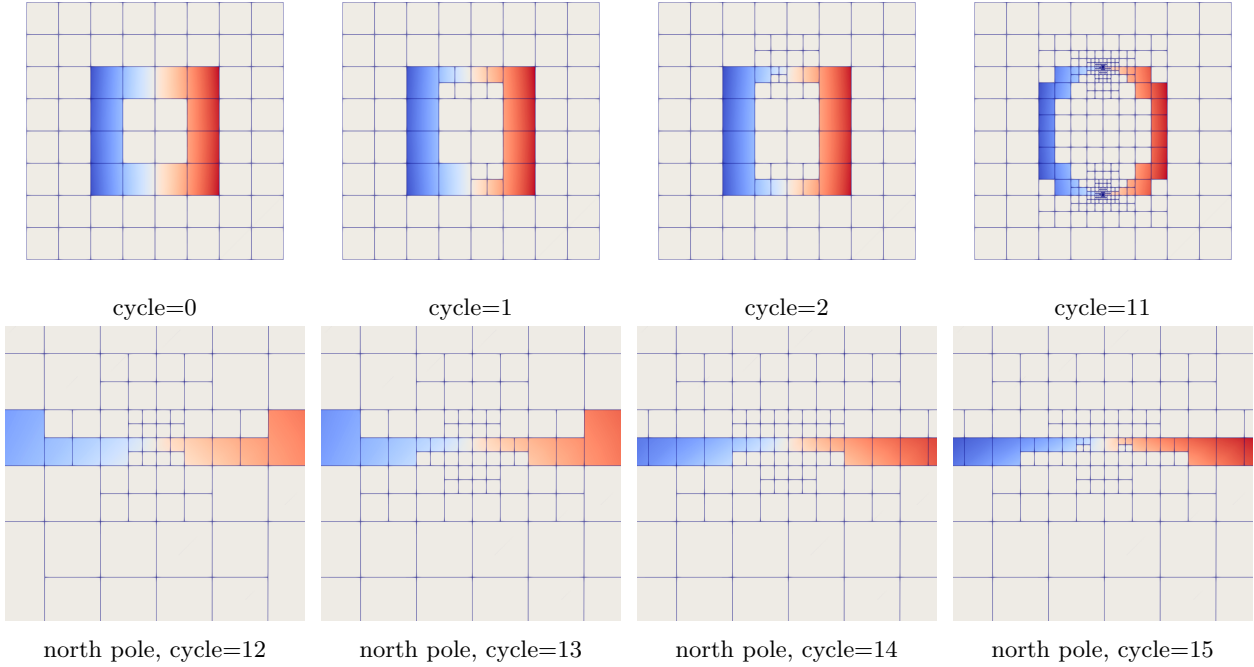


Figure 1: Snapshots of the mesh crosscuts at different cycles of the adaptive procedure from Section 4.2. The surface Γ_h is not shown. Active elements \mathcal{T}_h^Γ and the corresponding domain ω_h are colored by the values of the solution (51) with $\lambda = 0.4$. Vertical direction corresponds to OZ axis. Top: the whole domain $[-2, 2]^3$, with many cells remain coarse throughout the procedure. Bottom: closeup view of the north pole $(0, 0, 1)$ of the unit sphere where the gradient of the solution (51) blows up.

- Computation of the indicator (16) involves the same numerical integration procedures as used for (52).
- Although the forcing term f^e is not an $L^2(\Gamma_h)$ function, the integral on the right-hand side of (52) remains well-defined, provided that none of the surface quadrature nodes intersect the north or south poles when projected onto Γ .
- In the course of adaptive refinement some of inactive cells and some active cells not from \mathcal{T}_h^θ are refined so that the mesh remains graded.

4.4 Uniform refinement

The first example serves to motivate the adaptivity and to test our implementation of TraceFEM for V_h^1 and V_h^2 ambient spaces. We choose the exact solutions (51), $u_\lambda \in H^{1+\lambda}(\Gamma)$ with $\lambda = 1.0$, $\lambda = 0.7$ and $\lambda = 0.4$ and solve the discrete problems (10) with $k = 1$, $s_h(u, v) = s_h^{NV}(u, v)$, and stabilization parameter $\rho_S = 10h_S^{-1}$. The active domain ω_h is refined uniformly and the obtained solutions $u_h \in V_h^1$ are compared with the normal extension u^e of the exact solution $u \in H^{1+\lambda}(\Gamma)$. We evaluate the following surface error norms,

$$\|u_h - u^e\|_{L^2(\Gamma_h)}, \quad \|\nabla_{\Gamma_h} u_h - (\nabla_{\Gamma} u)^e\|_{L^2(\Gamma_h)} \quad (55)$$

and the results are presented in Figure 2. Optimal rates are observed for $\lambda = 1.0$, which corresponds to $u \in H^2(\Gamma)$, but, as λ decreases, the rates deteriorate in accordance with the regularity, $u_\lambda \in H^{1+\lambda}$, of the problem. Asymptotically, the rate h^λ is attained for the energy norm as it would be expected for fitted FEMs.

We conducted the same uniform refinement test using the gradient-jump face stabilization s_h^{JF} , and the results closely resemble those shown in Figure 2. Therefore, we have opted not to include an additional plot.

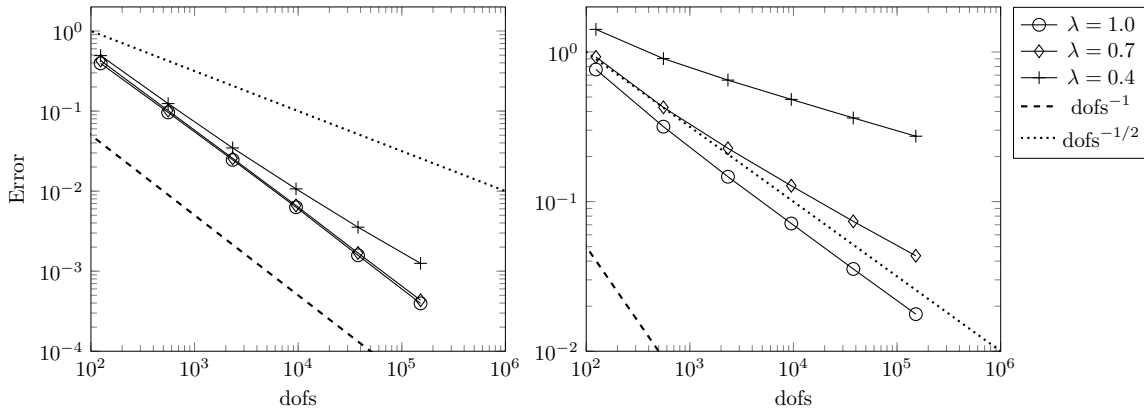


Figure 2: Uniform mesh refinement for different values of λ using the scheme (10) which is based on the Q_1 TraceFEM and is stabilized by (13). Left: $\|u_h - u^e\|_{L^2(\Gamma_h)}$ error. Right: $\|\nabla_{\Gamma_h} u_h - (\nabla_{\Gamma_h} u)^e\|_{L^2(\Gamma_h)}$ error. The exact solution u_λ is of low regularity, $u \in H^{1+\lambda}(\Gamma)$ only. The expected reduction of the convergence rates to h^λ , for the H^1 -seminorm is observed for $\lambda < 1$. The L^2 -norm error appears to be less sensitive to λ at least for the tested refinement levels.

Next, we repeated the test for the Q_2 family with $k = 2$ in V_h^k , employing the stabilizations s_h^{NV} and s_h^{JF2} . When $\lambda = 1$, the convergence rates are optimal and correspondent to a finite element space of second degree. However, in cases of low regularity where $\lambda < 1$, the rate of convergence attains h^λ only in the energy norm.

4.5 Efficiency indexes

In the numerical experiments we consider different notions of the efficiency. As usual, local efficiency indexes are computed for active cells $S_T \in \mathcal{T}_h^\Gamma$. These indices gauge how closely the actual error, $e_h = \nabla_{\Gamma_h} u_h - \nabla u^e$, is to the error indicator η on the cell. Accumulated over all cells, a reliable indicator estimates the error from above. The indicator is said to be efficient if the ratio of the indicator and the error, i.e. the efficiency index, is bounded from above independent of the discretization level.

We will consider three efficiency indexes which differ in the patch of neighboring cells contributing to the local error e_h for the cell S_T . To compute the indexes, one maximizes the following ratios over all cuts $T = S_T \cap \Gamma_h$,

$$I_1 = \max_T \frac{\eta(S_T)}{\|\xi_h\|_{\Gamma_h \cap \omega_{S_T}}}, \quad I_2 = \max_T \frac{\eta(S_T)}{\|\xi_h\|_{\Gamma_h \cap \omega_T}}, \quad I_3 = \max_T \frac{\eta_R(T)}{\|\xi_h\|_{\Gamma_h \cap S_T}} \quad (56)$$

Here $\xi_h = \nabla_{\Gamma_h} u_h - \nabla u^e$ is the energy error, ω_{S_T} is the patch of all active cells from ω_h which share at least a vertex with the cell S_T ; ω_T is the patch of all active cells from ω_h which share with the cell S_T a face intersected by Γ_h . Clearly, the efficiency index I_3 accumulates the error over a single cell S_T only and it is the sharpest way to characterize the indicator. The notion of efficiency given by I_3 is too stringent, as it is known that the corresponding index blows up numerically even for a fitted FEM. At the same time, the theory of a fitted adaptive FEM guarantees that the indicator is efficient if the error is accumulated over a patch of neighbors. This fact suggests that the indexes I_1 and I_2 are reasonable extensions of a similar notion to the unfitted finite element. The distinction between I_1 and I_2 lies in their dependence on the bulk mesh and the surface: in the former, the patch is based on the connectivity of the intersected cuts T , while in the latter, it relies on the connectivity of the bulk cells S_T .

Remark 4.1. Note that the error part in (56) does not include the stabilization s_h because we are interested in the surface error for a solution to a surface PDE. This is in contrast to the indicator $\eta(S_T)$ and to the natural discrete norm of (10) which include the stabilization s_h . One may question if adding the stabilization $s_h(u_h - u^e, u_h - u^e)$ to the denominator of indicators (56) can lead to a notion of efficiency which is more suitable to TraceFEM. As we found in our numerical experiments, such alternation does not change main

conclusions drawn from the numerical experiments. For these reasons, we present the numerical results using the efficiency indexes as defined in (56).

4.6 Efficiency and Reliability for the Q_1 elements

In this experiment, we assess the reliability and the efficiency of the indicator (53) using the Q_1 family of polynomials (9). Therefore, we choose a low-regularity solution (51), $u \in H^{1+\lambda}(\Gamma)$ with $\lambda = 0.4$, of the Laplace–Beltrami problem (3) posed on the unit sphere. We run the adaptive TraceFEM stabilized by $s_h = s_h^{JF}$ with $\sigma_F = 10$ and by $s_h = s_h^{NV}$ with $\rho_S = 10h_S^{-1}$ and evaluate surface errors (55).

The numerical results, as presented in the top panel of Figure 3, confirm the a posteriori analysis conducted in Section 3. Optimal rates are observed with both stabilizations, s_h^{NV} and s_h^{JF} , as shown in Figure 3, and fewer degrees of freedom appear to be needed while using s_h^{NV} to achieve comparable errors. Furthermore, in the plots of the bottom panel in Figure 3, we evaluate the efficiency indexes (56) corresponding to several notions of efficiency discussed in Section 4.5. The indexes I_1 and I_2 suggest the efficiency of the indicators for Q_1 adaptive TraceFEM.

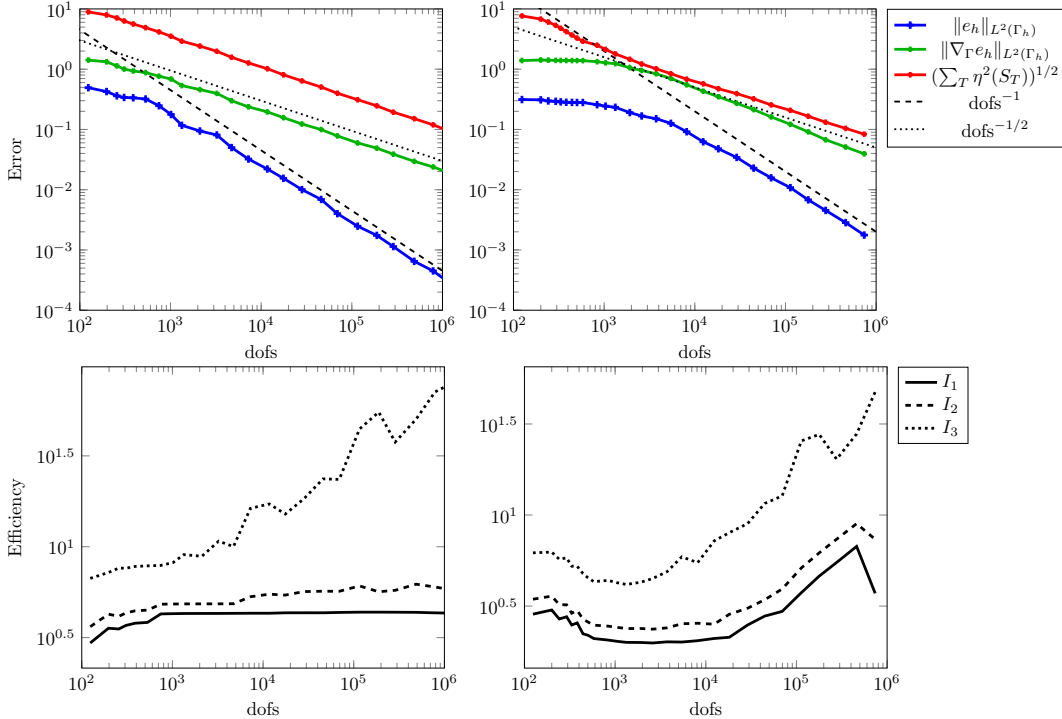


Figure 3: Adaptive refinement with $\theta = 0.5$ using the indicator (16) for the Q_1 TraceFEM. Left: s_h^{NV} stabilization with $\rho_S = 10h_S^{-1}$. Right: s_h^{JF} stabilization with $\sigma_F = 10$. Top: surface errors (55) for $e_h = u_h - u^e$ and the global estimator $(\sum_T \eta^2(S_T))^{1/2}$. Bottom: efficiency indexes (56) for different patches of neighbors. The exact solution $u \in H^{1+\lambda}(\Gamma)$ with $\lambda = 0.4$ is given by (51) on the unit sphere Γ . We observe that the indicator (16) is reliable and efficient for Q_1 TraceFEM with both stabilizations.

4.7 Efficiency and Reliability for the Q_2 elements

We proceeded to repeat the experiment for the Q_2 TraceFEM, employing the discrete space V_h^2 for both the solution u_h and the surface approximation Γ_h , following the same adaptive algorithm outlined in Section 4.2. In this case, for the gradient-jump face stabilization, the s_h^{JF} form was replaced by the s_h^{JF2} form with $\sigma_F = 10$. As shown in the top panel of Figure 4, the Q_2 TraceFEM with gradient-jump face stabilization exhibits optimal convergence rates in the L_2 and H_1 norms, while the Q_2 TraceFEM with normal-gradient

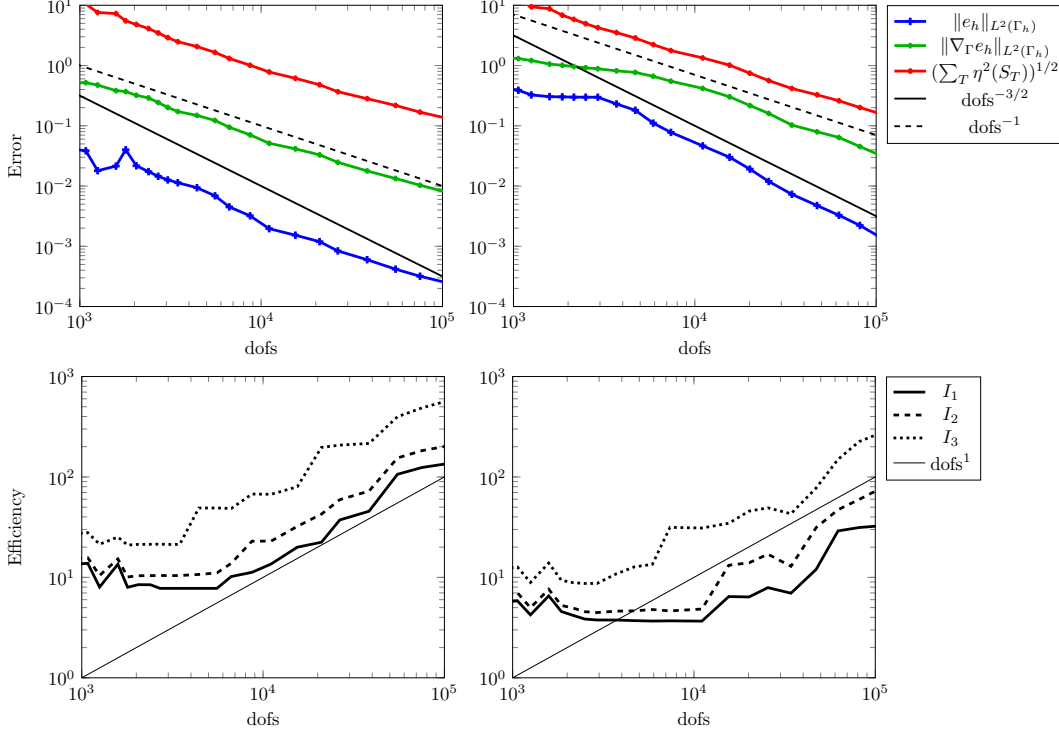


Figure 4: Adaptive refinement with $\theta = 0.5$ using the indicator (16) for the Q_2 TraceFEM. Left: s_h^{NV} stabilization with $\rho_S = 10h_S^{-1}$. Right: s_h^{JF2} stabilization with $\sigma_F = \tilde{\sigma}_F = \tilde{\sigma}_\Gamma = \sigma_\Gamma = 10$. Top: surface errors (55) for $e_h = u_h - u^e$ and the global estimator $(\sum_T \eta^2(S_T))^{1/2}$. The exact solution $u \in H^{1+\lambda}(\Gamma)$ with $\lambda = 0.4$ is given by (51) on the unit sphere Γ . The indicator (16) is reliable in the energy norm for the Q_2 TraceFEM with both stabilizations. The growth of all indexes shown on the bottom panels suggest the lack of efficiency. Unlike the energy norm, for which the indicator was designed for, convergence rate in L^2 norm appears to be suboptimal for the s_h^{NV} stabilization.

volume stabilization shows almost optimal rates in the H^1 norm (which is the goal of the suggested indicator (16)) and suboptimal rates in the L_2 norm. Nevertheless, similar to the Q_1 case, the normal-gradient volume stabilization attains considerably smaller errors in both norms for the same number of unknowns. Unlike the Q_1 scenario, the efficiency indexes in the Q_2 case exhibit linear growth with the number of degrees of freedom, as depicted in the bottom panel of Figure 4.

4.7.1 Effect of the stabilization parameter in s_h^{JF2}

It was observed in [3] that the performance of the stabilization s_h^{JF2} defined in (12) is sensitive to the choice of the stabilization parameters. We would like to demonstrate how different values of σ_F affect the adaptive TraceFEM with indicator (53).

We did not observe improvements in efficiency by tuning the parameter σ_F in Figure 4, where we used $\sigma_F = 10$. To illustrate this point, we present the results of adaptive TraceFEM for two extreme values of the stabilization parameter: $\sigma_F = 0.1$ and $\sigma_F = 1000$, as shown in Figure 5. Similar to Figure 4, the convergence rates are nearly optimal for both extreme values. However, when $\sigma_F = 1000$, achieving the same level of accuracy requires more degrees of freedom compared to the case of $\sigma_F = 0.1$.

This behavior of errors is consistent with what is typically observed during uniform refinement. In the adaptive setting, the indicator η includes the stabilization, and when $\sigma_F = 1000$, the estimator focuses on reducing the contribution of the stabilization $s_h(u_h, u_h)$ to the error functional $\|e_h\|$, as illustrated in the right panels of Figure 5.

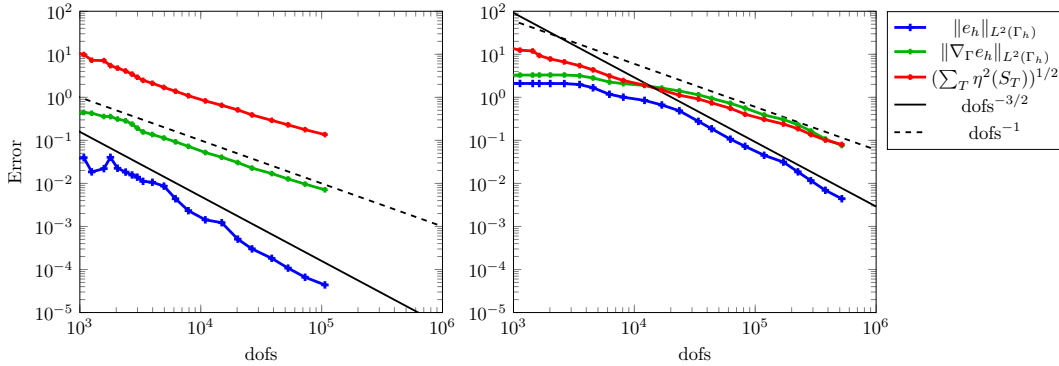


Figure 5: The effect of the stabilization parameter σ_F on the adaptive refinement in Figure 4. Left: $\sigma_F = 0.1$. Right: $\sigma_F = 1000$. Surface errors (55) for $e_h = u_h - u^e$ and the global estimator $(\sum_T \eta^2(S_T))^{1/2}$ are shown. We observe that decreasing the stabilization parameter does not improve the lack of efficiency while increasing it postpones the asymptotic regime of convergence.

5 Conclusions

In this paper, we explore the application of adaptive stabilized TraceFEM for the first time. We focus on solving an elliptic problem on a fixed surface using the two lowest-order continuous finite element spaces based on Q_1 and Q_2 elements. For each family, we investigate both the gradient-jump face and normal-gradient volume stabilizations.

Our analysis demonstrates that the error indicator in the proposed adaptive TraceFEM is reliable, and our numerical tests confirm the theoretical findings. Specifically, for Q_1 elements, a reasonable choice for low-regularity solutions, we establish a robust and practical adaptive stabilized TraceFEM scheme. In the case of Q_2 , the efficiency indexes grow proportionally with the number of active degrees of freedom.

Another significant contribution of this paper relates to the practical implementation of the proposed indicator. Rather than computing gradient jumps along one-dimensional curvilinear edges between surface patches, which can be computationally intensive due to the implicit surface description in TraceFEM, we evaluate gradient jumps on two-dimensional faces between bulk cells. This approach simplifies the implementation of the indicator.

In conclusion, we recommend caution when using the Q_2 element in adaptive stabilized TraceFEM schemes, while the Q_1 element provides a highly robust adaptive method.

Acknowledgments

The author T.H. was partially supported by the National Science Foundation Award DMS-2028346, OAC-2015848, EAR-1925575, and by the Computational Infrastructure in Geodynamics initiative (CIG), through the NSF under Award EAR-0949446, EAR-1550901, EAR-2149126 via the University of California – Davis. The author M.O. was partially supported by the National Science Foundation under award DMS-2309197. The author V.Y. was partially supported by the National Science Foundation Award OAC-2015848 and EAR-1925575. Clemson University is acknowledged for generous allotment of compute time on Palmetto cluster.

References

- [1] M. A. Olshanskii and A. Reusken, “Trace finite element methods for pdes on surfaces,” in *Geometrically Unfitted Finite Element Methods and Applications: Proceedings of the UCL Workshop 2016*, pp. 211–258, Springer, 2017.

- [2] E. Burman, P. Hansbo, and M. G. Larson, “A stabilized cut finite element method for partial differential equations on surfaces: the laplace–beltrami operator,” *Computer Methods in Applied Mechanics and Engineering*, vol. 285, pp. 188–207, 2015.
- [3] M. G. Larson and S. Zahedi, “Stabilization of high order cut finite element methods on surfaces,” *IMA Journal of Numerical Analysis*, vol. 40, no. 3, pp. 1702–1745, 2020.
- [4] A. Demlow and M. Olshanskii, “An adaptive surface finite element method based on volume meshes,” *SIAM J. Numer. Anal.*, vol. 50, pp. 1624–1647, 2012.
- [5] A. Y. Chernyshenko and M. A. Olshanskii, “An adaptive octree finite element method for PDEs posed on surfaces,” *Computer Methods in Applied Mechanics and Engineering*, vol. 291, pp. 146–172, July 2015.
- [6] M. A. Gharbi, D. Seč, T. Lopez-Leon, M. Nobili, M. Ravnik, S. Žumer, and C. Blanc, “Microparticles confined to a nematic liquid crystal shell,” *Soft Matter*, vol. 9, no. 29, pp. 6911–6920, 2013.
- [7] Y. Hu, Y. Qu, and P. Zhang, “On the disclination lines of nematic liquid crystals,” *Communications in Computational Physics*, vol. 19, no. 2, pp. 354–379, 2016.
- [8] V. Koning, T. Lopez-Leon, A. Darmon, A. Fernandez-Nieves, and V. Vitelli, “Spherical nematic shells with a threefold valence,” *Physical Review E*, vol. 94, no. 1, p. 012703, 2016.
- [9] M. Nestler and A. Voigt, “Active nematodynamics on curved surfaces – the influence of geometric forces on motion patterns of topological defects,” *Communications in Computational Physics*, vol. 31, no. 3, pp. 947–965, 2022.
- [10] G. Dziuk, “Finite elements for the Beltrami operator on arbitrary surfaces,” in *Partial Differential Equations and Calculus of Variations (S. Hildebrandt and R. Leis eds)*. *Lecture Notes in Mathematics*, vol. 1357, pp. 142–155, Berlin: Springer, 1988.
- [11] C. Bernardi and R. Verfürth, “Adaptive finite element methods for elliptic equations with non-smooth coefficients,” *Numerische Mathematik*, vol. 85, pp. 579–608, 2000.
- [12] M. Olshanskii, A. Reusken, and J. Grande, “A finite element method for elliptic equations on surfaces,” *SIAM J. Numer. Anal.*, vol. 47, pp. 3339–3358, 2009.
- [13] E. Burman, P. Hansbo, and M. G. Larson, “A stabilized cut finite element method for partial differential equations on surfaces: The Laplace–Beltrami operator,” *Computer Methods in Applied Mechanics and Engineering*, vol. 285, pp. 188–207, 2015.
- [14] E. Burman, P. Hansbo, M. G. Larson, and A. Massing, “Cut finite element methods for partial differential equations on embedded manifolds of arbitrary codimensions,” *ESAIM: Mathematical Modelling and Numerical Analysis*, vol. 52, no. 6, pp. 2247–2282, 2018.
- [15] J. Grande, C. Lehrenfeld, and A. Reusken, “Analysis of a high-order trace finite element method for pdes on level set surfaces,” *SIAM Journal on Numerical Analysis*, vol. 56, no. 1, pp. 228–255, 2018.
- [16] T. Aubin, *Nonlinear analysis on manifolds, Monge-Ampere equations*, vol. 252. Springer, 1982.
- [17] P. Hansbo, M. G. Larson, and S. Zahedi, “Characteristic cut finite element methods for convection–diffusion problems on time dependent surfaces,” *Computer Methods in Applied Mechanics and Engineering*, vol. 293, pp. 431–461, 2015.
- [18] E. Burman, P. Hansbo, M. G. Larson, and S. Zahedi, “Cut finite element methods for coupled bulk–surface problems,” *Numerische Mathematik*, vol. 133, no. 2, pp. 203–231, 2016.
- [19] S. Zahedi, “A space-time cut finite element method with quadrature in time,” in *Geometrically Unfitted Finite Element Methods and Applications: Proceedings of the UCL Workshop 2016* (S. Bordas, E. Burman, M. Larson, and M. Olshanskii, eds.), pp. 281–306, Springer, 2017.

- [20] C. Lehrenfeld, M. A. Olshanskii, and X. Xu, “A stabilized trace finite element method for partial differential equations on evolving surfaces,” *SIAM Journal on Numerical Analysis*, vol. 56, no. 3, pp. 1643–1672, 2018.
- [21] V. Yushutin, A. Quaini, and M. Olshanskii, “Numerical modeling of phase separation on dynamic surfaces,” *Journal of Computational Physics*, vol. 407, p. 109126, 2020.
- [22] M. Olshanskii, X. Xu, and V. Yushutin, “A finite element method for Allen–Cahn equation on deforming surface,” *Computers & Mathematics with Applications*, vol. 90, pp. 148–158, 2021.
- [23] M. A. Olshanskii, A. Reusken, and A. Zhiliakov, “Tangential Navier–Stokes equations on evolving surfaces: Analysis and simulations,” *Mathematical Models and Methods in Applied Sciences*, pp. 1–36, 2022.
- [24] M. A. Olshanskii, A. Reusken, and P. Schwering, “An Eulerian finite element method for tangential Navier–Stokes equations on evolving surfaces,” *arXiv preprint arXiv:2302.00779*, 2023.
- [25] A. Demlow and G. Dziuk, “An adaptive finite element method for the Laplace–Beltrami operator on implicitly defined surfaces,” *SIAM J. Numer. Anal.*, vol. 45, pp. 421–442, 2007.
- [26] A. Hansbo, P. Hansbo, and M. G. Larson, “A finite element method on composite grids based on Nitsche’s method,” *ESAIM: Mathematical Modelling and Numerical Analysis*, vol. 37, pp. 495–514, 2003.
- [27] V. Heuveline and F. Schieweck, “H1-interpolation on quadrilateral and hexahedral meshes with hanging nodes,” *Computing*, vol. 80, no. 3, pp. 203–220, 2007.
- [28] D. Arndt, W. Bangerth, M. Bergbauer, M. Feder, M. Fehling, J. Heinz, T. Heister, L. Heltai, M. Kronbichler, M. Maier, P. Munch, J.-P. Pelteret, B. Turcksin, D. Wells, and S. Zampini, “The deal.II library, version 9.5,” *Journal of Numerical Mathematics*, vol. 31, no. 3, pp. 231–246, 2023.
- [29] D. Arndt, W. Bangerth, D. Davydov, T. Heister, L. Heltai, M. Kronbichler, M. Maier, J.-P. Pelteret, B. Turcksin, and D. Wells, “The deal.II finite element library: Design, features, and insights,” *Computers & Mathematics with Applications*, vol. 81, pp. 407–422, 2021.
- [30] R. I. Saye, “High-order quadrature methods for implicitly defined surfaces and volumes in hyperrectangles,” *SIAM Journal on Scientific Computing*, vol. 37, no. 2, pp. A993–A1019, 2015.